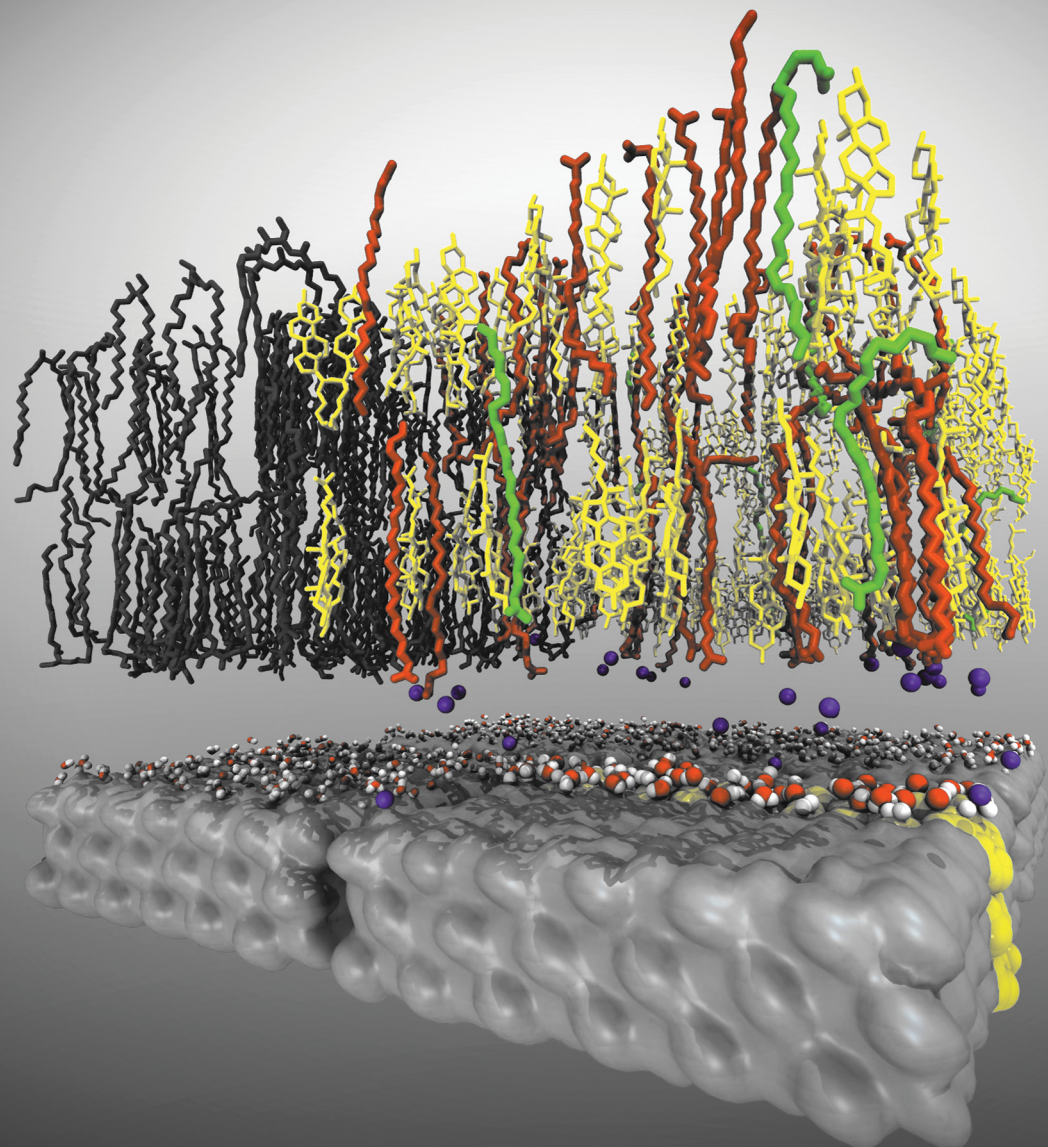


# Soft Matter

rsc.li/soft-matter-journal



ISSN 1744-6848



Cite this: *Soft Matter*, 2021,  
17, 6507

## How to control interactions of cellulose-based biomaterials with skin: the role of acidity in the contact area†

Andrey A. Gurtovenko \*<sup>a</sup> and Mikko Karttunen <sup>abcd</sup>

Being able to control the interactions of biomaterials with living tissues and skin is highly desirable for many biomedical applications. This is particularly the case for cellulose-based materials which provide one of the most versatile platforms for tissue engineering due to their strength, biocompatibility and abundance. Achieving such control, however, requires detailed molecular-level knowledge of the dominant interaction mechanisms. Here, we employed both biased and unbiased atomic-scale molecular dynamics simulations to explore how cellulose crystals interact with model *stratum corneum* bilayers, ternary mixtures of ceramides, cholesterol, and free fatty acids. Our findings show that acidity in the contact area directly affects binding between cellulose and the *stratum corneum* bilayer: Protonation of free fatty acids in the bilayer promotes attractive cellulose–bilayer interactions. We identified two major factors that control the cellulose–skin interactions: (i) the electrostatic repulsion between a cellulose crystal and the charged (anionic due to deprotonated fatty acids) surface of a *stratum corneum* bilayer and (ii) the cellulose–*stratum corneum* hydrogen bonding. When less than half of the fatty acids in the bilayer are protonated, the first factor dominates and there is no binding to skin. At a larger degree of fatty acid protonation the cellulose–*stratum corneum* hydrogen bonding prevails yielding a tight binding. Remarkably, we found that ceramide molecules are the key component in hydrogen bonding with cellulose. Overall, our findings highlight the critical role of fatty acid protonation in biomaterial–*stratum corneum* interactions and can be used for optimizing the surface properties of cellulose-based materials aimed at biomedical applications such as wound dressings.

Received 24th April 2021,  
Accepted 2nd June 2021

DOI: 10.1039/d1sm00608h

rsc.li/soft-matter-journal

## 1 Introduction

Cellulose-based biomaterials have attracted much attention due to their potential for numerous applications in medicine and biotechnology.<sup>1–6</sup> This potential originates from the inherent properties of cellulose: it comes from natural sources and is abundant, biocompatible, nontoxic, and cheap.<sup>7</sup> In many important applications, for example in tissue engineering,<sup>8,9</sup> bone implants,<sup>10</sup> hemodialysis membranes,<sup>11,12</sup> and wound dressing,<sup>13</sup> there is a direct contact of the biomaterial with tissues and skin. In particular, the biomaterial–skin interactions are especially critical

for wound dressing as an excessive adherence of dressing to the wound/skin could lead to tissue trauma. Therefore, it is highly desirable to fully understand the interactions between cellulose-based materials and skin, the factors that control such interactions, as well as the impact of the biomaterial on the outer layers of the skin. Such molecular-level knowledge may also be relevant to the long-standing problem of the needleless transdermal drug delivery.<sup>14</sup>

Computer simulations along with high (atomic-scale) resolution models have become an irreplaceable tool for gaining molecular-level insight into the behaviors of complex systems, which is not easily available using experimental techniques. In the current context, we recently published a series of computational papers on the interactions of cellulose-based materials with model plasma membranes.<sup>15–17</sup> Our findings highlighted a crucial role of hydrogen bonding of cellulose with model cell membranes<sup>15,16</sup> as well as the impact of cellulose's surface modification.<sup>17</sup>

Given the tremendous importance of the biomaterial–skin interactions, here we extend our earlier computational studies to the outer layer of the skin, the *stratum corneum* (SC). We employ atomic-scale molecular dynamics (MD) simulations to explore,

<sup>a</sup> Institute of Macromolecular Compounds, Russian Academy of Sciences, Bolshoi Prospect V.O. 31, St. Petersburg 199004, Russia. E-mail: a.gurtovenko@gmail.com; Web: biosimu.org; Tel: +7-812-3285601

<sup>b</sup> Department of Chemistry, The University of Western Ontario, 1151 Richmond Street, London, Ontario N6A 3K7, Canada

<sup>c</sup> Department of Applied Mathematics, The University of Western Ontario, 1151 Richmond Street, London, Ontario N6A 5B7, Canada

<sup>d</sup> The Centre for Advanced Materials and Biomaterials Research, The University of Western Ontario, 1151 Richmond Street, London, Ontario N6A 5K7, Canada

† Electronic supplementary information (ESI) available. See DOI: 10.1039/d1sm00608h

for a first time, the interactions between a crystalline cellulose-based material and model biomembranes whose composition matches that of the lipid matrix of the *stratum corneum*. This aim is to unlock the molecular mechanisms responsible for biomaterial binding to skin and to identify the means to control such binding.

It is well established that the *stratum corneum* represents a brick-and-mortar arrangement, in which corneocytes (bricks) are surrounded by the multilamellar extracellular lipid matrix (mortar).<sup>18,19</sup> This lipid matrix is considered as the main permeation pathway of the skin and it is composed of three major components: ceramides, cholesterol and free fatty acids.<sup>20–22</sup> The ratios of these three components can vary considerably. Furthermore, fatty acids with different chain lengths and over a hundred of different ceramide types are known to constitute the SC lipid matrix.<sup>23,24</sup> Given the complexity of the real SC layers, both experiments and computer simulations often focus on much more simplified model membranes that are composed of the abundant types of ceramides and fatty acids. We would like to mention, however, that simulations with more complex models for SC have recently started to emerge.<sup>25</sup>

Earlier atomic-scale MD simulations of the SC solely considered bilayers built from ceramide molecules.<sup>26–28</sup> The state-of-the-art standard in computer modeling of the SC uses mixtures of ceramides, fatty acids and cholesterol, and computational studies have focused on the effects of temperature, relative ratios of different components, ceramide tail lengths, and fatty acid protonation on the structure and properties of model SC lipid bilayers.<sup>29–33</sup> As far as the protonation state of fatty acids (FAs) in the SC is concerned, simulations have thus far explored only two opposite situations, *i.e.*, when all the FAs in the SC bilayer were either protonated<sup>29–33</sup> or deprotonated.<sup>31,32</sup> However, the acid mantle within the outer SC layers could lead to a simultaneous presence of both protonated and deprotonated forms of free FAs in the upper part of the SC.<sup>34</sup> In turn, a pH gradient in deeper SC layers gradually suppress FA protonation, so that the interior of the SC most likely consists of deprotonated FAs only.<sup>31,34</sup>

Protonation of free FAs directly affects the overall charge of the SC membrane and can therefore play an essential role in skin's adhesive properties. As we proceed to show, the FA protonation state (or the acidity in the contact area) controls the interactions between the SC layer and the cellulose-based material. In our atomic-scale MD simulations we vary systematically the protonation of free FAs in the SC lipid bilayer and demonstrate that increasing FA protonation promotes binding of the biomaterial to the skin. These findings could be employed for optimizing the surface properties of the cellulose-based materials aimed at the use as wound dressing.

## 2 Models and methods

We performed atomic-scale MD simulations of a cellulose (CEL) crystal interacting with a model SC lipid bilayer, see Fig. 1. Similar to our previous studies,<sup>15–17</sup> the crystal is based on the structure of I $\beta$  cellulose<sup>35</sup> and built from cellulose chains of the

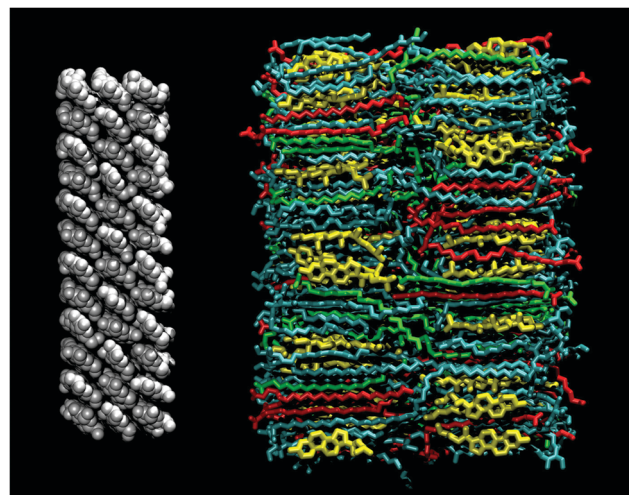
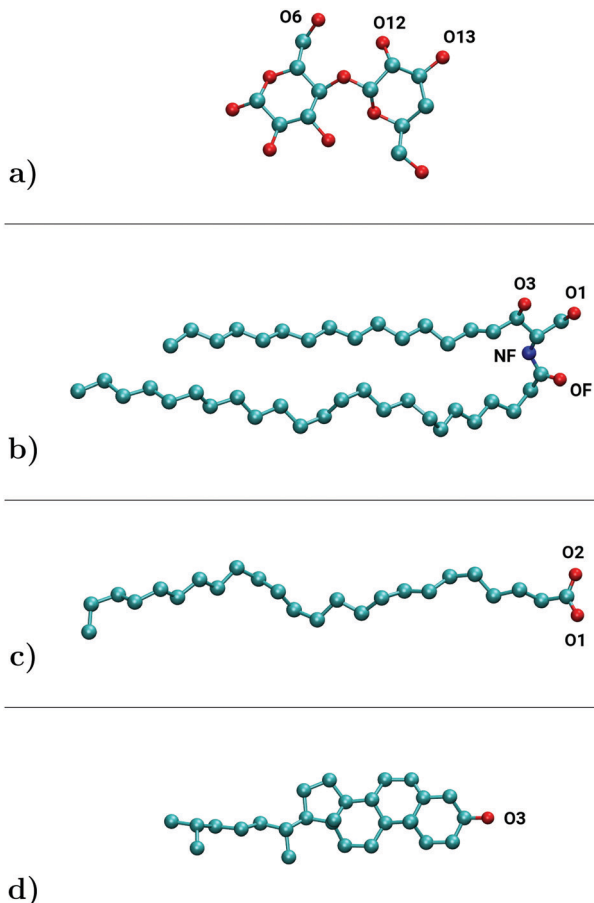


Fig. 1 Snapshot of a cellulose–SC bilayer system. The cellulose crystal is shown in white, ceramide (Cer) in cyan, cholesterol (Chol) in yellow, deprotonated fatty acids (LA) in red, and protonated fatty acids (LAP) in green. Water and ions are not shown for clarity.

same length (6 cellobiose units in each chain). The cellulose crystal comprises three layers with 12 chains in each layer. Since the focus is on the interactions between the skin and the surface of a cellulose crystal, the inner structure of the crystal (*i.e.* heavy atoms of sugar rings except hydroxyl and hydroxymethyl groups) was kept rigid by imposing position restraints.<sup>15–17</sup>

As a model SC lipid bilayer, we considered an equimolar mixture of *N*-lignoceroylsphingosine (Cer), lignoceric acid (in the deprotonated (LA) and protonated (LAP) forms) and cholesterol (Chol), see Fig. 1 and 2. These types of ceramides and free fatty acids are considered to be the most abundant ones in the SC and have been used in computational studies of model SC lipid membranes.<sup>30,31,33</sup> A SC bilayer comprises 106 molecules of each component (Cer, LA (LAP), and Chol), resulting in a total of 318 molecules. The proportion of protonated FAs was varied systematically from 0% to 100%, see Table 1. We considered five SC bilayers with 0, 25, 50, 75, and 100% of protonated fatty acids; protonated (LAP) and deprotonated (LA) fatty acids were evenly distributed over the opposite bilayer leaflets. Free-standing SC bilayers were hydrated with water; the number of water molecules was varied from 9800 to 12 700, depending on the number of deprotonated (anionic) LAs. An appropriate number of K<sup>+</sup> counter-ions was added into the systems to keep them charge-neutral. The systems here are fully hydrated in order to keep them comparable to previous studies.<sup>15–17</sup> Typical hydration level of SC is, however, low. For example, Warner *et al.*<sup>36</sup> reported 15 wt% which is in line with other measurements; the effects of different levels of hydration on SC properties have been extensively studied by Silva *et al.*<sup>37</sup> and Mojumdar *et al.*<sup>38</sup> Simulations have generally used somewhat larger values than the experimental ones, one of the reasons being that low hydration has been shown to lead to instabilities in some cases. For example, Höltje *et al.* reported that simulations at the level of 2.5 waters/lipid ( $\approx$  10 wt%) lead to unstable simulations and as a result they used 5–6 waters per lipid.<sup>39</sup> This number is



**Fig. 2** Chemical structures and numbering of the key atoms of the constituents of the “cellulose–stratum corneum” systems: (a) cellulose dimer, (b) *N*-lignoceroylsphingosine, Cer, (c) lignoceric acid, LA/LAP (protonated and deprotonated fatty acids differ in having/not having a hydrogen atom at the oxygen O1), and (d) cholesterol, Chol. Hydrogen atoms are not shown for clarity.

**Table 1** Simulated cellulose–SC bilayer systems

System	LAP content [%]	Simulation time [ns]
CEL-SC-P0	0	600
CEL-SC-P25	25	600
CEL-SC-P50	50	600
CEL-SC-P75	75	600
CEL-SC-P100	100	600
CEL-SC-P0-PMF	0	$36 \times 100$
CEL-SC-P25-PMF	25	$36 \times 100$
CEL-SC-P50-PMF	50	$36 \times 100$
CEL-SC-P75-PMF	75	$36 \times 100$
CEL-SC-P100-PMF	100	$36 \times 100$
CEL-SC-P25-KCl-PMF	25	$36 \times 100$
CEL-SC-P50-KCl-PMF	50	$36 \times 100$

similar to Wang and Klauda.<sup>25</sup> In other cases limitations have been overcome by using layered systems such that the middle water layer is very thin yielding a very low hydration number in that layer while the outer surfaces (dual bilayer structure) have full hydration.<sup>33</sup>

In both biased and unbiased MD simulations a cellulose crystal and SC lipid bilayer were placed parallel to each other in

the *x*-*y* plane at a certain distance between their centers of masses (COMs) in the *z*-direction, see Fig. 1. The systems were solvated in water (from 12 300 to 13 200 H<sub>2</sub>O molecules were added) and neutralized with K<sup>+</sup> counterions. The total number of atoms in the CEL–SC systems varied from 75 500 to 78 000. The sizes of the cellulose crystals and SC lipid bilayers were chosen such that the SC bilayers had larger surface areas compared to that of the cellulose crystal. This ensured that the SC bilayer could move freely with respect to the surface of the crystal. Such an approach was proposed in ref. 16 and it allows one to overcome the limitations of lipid bilayers on a solid support.<sup>15,40–42</sup>

The CHARMM35 force field,<sup>43,44</sup> was used for cellulose while the CHARMM36 was employed for ceramides, free fatty acids, and cholesterol.<sup>31,45,46</sup> The CHARMM version of the TIP3P model was used for water.<sup>47</sup> The MD simulations were performed in the *NPT* ensemble (*T* = 310 K and *P* = 1 bar) using the Gromacs 5.1.4 simulation suite.<sup>48</sup> Equilibration runs were carried out using the velocity-rescaling thermostat<sup>49</sup> and the Berendsen barostat.<sup>50</sup> For production we switched to the Nosé–Hoover thermostat<sup>51,52</sup> and the Parrinello–Rahman barostat;<sup>53</sup> Shirts<sup>54</sup> has shown that both the v-rescale and Nosé–Hoover thermostat as well as the Parrinello–Rahman barostat perform well and produce the correct distributions, see also the discussion regarding thermostats and barostats by Wong-ekkabut and Karttunen.<sup>55</sup> Cellulose crystal, SC lipid bilayer, and water with ions were separately coupled to the thermostat; the semi-isotropic pressure coupling was employed. The P-LINCS constraint algorithm was applied to all bonds with hydrogen atoms.<sup>56</sup> The Lennard-Jones interactions were cut off at 1.2 nm. Following the original parameterization for this force field,<sup>45</sup> the forces were smoothly switched to zero between 1.0 and 1.2 nm. The electrostatic interactions were handled with the particle–mesh Ewald (PME) method.<sup>57</sup> Periodic boundary conditions were applied in all directions and the time step was set to 2 fs.

The initial structure of the cellulose crystal was taken from our previous studies.<sup>16,17</sup> The SC lipid bilayers consisting of equimolar mixture of Cer, fatty acids (LAs, LAPs, or both), and Chol were generated using the CHARMM-GUI Membrane Builder.<sup>58,59</sup> After hydration and short pre-equilibration, each free-standing SC lipid bilayer was simulated for 500 ns. The well-equilibrated structures of the SC bilayers were then used for building up the cellulose–bilayer systems.

The umbrella sampling technique was used to evaluate the free energy of binding of the SC lipid bilayer to the cellulose crystal.<sup>60</sup> Here we closely follow the protocol developed in our previous studies.<sup>16,17</sup> The initial COM distance between the SC bilayer and the cellulose crystal was set to 6.8 nm. To generate a set of configurations (“windows”) for umbrella sampling we used the Gromacs pull code:<sup>48,61</sup> the SC lipid bilayer was pulled toward the crystal surface with a velocity of 0.0001 nm ps<sup>-1</sup> and a force constant of 1000 kJ mol<sup>-1</sup> nm<sup>-2</sup>. Both the velocity and force constant were increased to 0.05 nm ps<sup>-1</sup> and 3000 kJ mol<sup>-1</sup> nm<sup>-2</sup>, when a bilayer–cellulose contact was established.<sup>16,17</sup> After the pulling process was performed, 36 windows were extracted from the trajectory with the COM cellulose–bilayer distance in the range

of 3.3–6.8 nm; the spacing between windows was set to 0.1 nm. Each window was simulated for 100 ns with the force constant of 3000 kJ mol<sup>-1</sup> nm<sup>-2</sup> and the last 80 ns of each trajectory was used for computing the free-energy by the weighted histogram analysis (WHAM) method.<sup>62</sup> The errors were evaluated using the bootstrapping method.<sup>61</sup> To estimate the influence of salt ions on the calculated free energy profiles, we added 150 mM of KCl to the cellulose–SC bilayer systems with 25 and 50% of protonated fatty acids and repeated the umbrella sampling calculations, see the CEL–SC–P25–KCl–PMF and CEL–SC–P50–KCl–PMF systems in Table 1. The accumulated simulation time of the biased MD simulations amounted to 25 μs.

In addition to the biased simulations, we also performed a series of unbiased MD simulations of five salt-free CEL–SC systems. The COM distance of the cellulose crystal and the SC lipid bilayer was 3.8 nm as that is the distance when they establish contact. The corresponding umbrella window was used as the starting configuration for the unbiased simulations. After short (20 ns) pre-equilibration, all five cellulose–SC bilayer systems were simulated for 600 ns, see Table 1. The last 300 ns were used for data analysis. To monitor the equilibration, we analyzed the time evolution of the distance between the centers of masses of the SC lipid bilayers and the cellulose crystal along the bilayer normal, see Section 3.2. The accumulated simulation time of the unbiased simulations amounted to 3 μs, Table 1.

### 3 Results and discussion

#### 3.1 Free-standing stratum corneum bilayers

Before considering the cellulose–SC bilayer systems, we first discuss briefly the free-standing SC lipid bilayers. The bilayers comprise an equimolar mixture of ceramides, cholesterol and free fatty acids. Unlike in previous computational studies of SC lipid bilayers, here we varied systematically the content of protonated FAs (LAPs) and considered five SC bilayers with LAP contents of 0, 25, 50, 75, and 100%. We note that – to the best of our knowledge – only SC lipid bilayers with fully protonated<sup>29–33</sup> (LAP content equals 100%) or fully deprotonated<sup>31,32</sup> (LAP content is 0%) FAs have been simulated thus far.

Each free-standing SC bilayer was simulated for 500 ns and the last 100 ns were used for a data analysis. In particular, we calculated the area per lipid for each bilayer and found that it amounted to  $0.325 \pm 0.001$  nm<sup>2</sup> and did not depend on FA protonation. Importantly, the area per lipid is in an excellent agreement with the values reported in previous simulation studies, in which the authors considered equimolar mixtures of Cer, Chol, and LA (LAP) with LAP content of either 0 or 100% using the same force field (CHARMM36).<sup>31,32</sup>

In Fig. S1 (ESI†) we show the component-wise mass density profiles for the free-standing SC bilayers. The SC bilayer is characterized by the hydrophobic interior which is impenetrable for water. The mass density profile of ceramides has a structured shape with pronounced maxima at the lipid/water interface and in the middle of the bilayer, the latter being a signature of interdigititation of long fatty acid chains of Cer (24 carbon atoms).

Cholesterol molecules are localized in the middle of the individual bilayer leaflets; their position is not sensitive to FA protonation. The most striking differences in the mass density profiles are observed for deprotonated and protonated fatty acids (LAs and LAPs). The distribution of LA chains is noticeably wider compared to their LAP counterparts as long as the LAP content is smaller than 75%. In other words, anionic LAs are elongated towards to the lipid/water interface, where they interact with the K<sup>+</sup> counterions adsorbed on the bilayer surface. Due to this elongation towards the aqueous phase, the deprotonated LA chains are less involved in interdigitation in the middle of the bilayer as compared to LAP chains. This is best illustrated by the mass density distribution for the SC bilayer with an equimolar mixture of LAs and LAPs, see Fig. S1 (ESI†). The mass density profiles are also in qualitative agreement with observations from cholesterol-lignoceric acid-distearylphosphatidylcholine (DSPC) systems.<sup>63</sup>

In addition to the density profiles, we also analyzed the electrostatic properties of free-standing SC bilayers. To this end, we calculated the electrostatic potential of the SC bilayers by integrating the Poisson equation, see ref. 64 for details. Each potential profile was then symmetrized with respect to the center of mass of the bilayer, resulting in the electrostatic potential of one leaflet. In Fig. S2 (ESI†) we present the electrostatic potential for all considered SC bilayers. Overall, the shape of the potential profile turned out to be similar to that reported for multicomponent phospholipid membranes.<sup>65</sup> The potential of a SC bilayer in aqueous solution is negative with respect to the bilayer center. Interestingly, the drop in the electrostatic potential across a bilayer leaflet systematically increases with LAP content from 0.63 to 0.90 V for SC bilayers with fully deprotonated and fully protonated FAs, respectively (see Fig. S2, ESI†). The analysis of various component-wise contributions to the electrostatic potential showed that the contributions of both ceramides and cholesterol molecules are negative, comparable and insensitive to the LAP content, see Fig. S3 (ESI†). In turn, the contribution of LAPs is small and positive. Negatively charged head groups of LAs and the positively charged K<sup>+</sup> ions adsorbed on the bilayers form dipoles at the lipid/water interface giving rise to a noticeable reorientation of water molecules. As a result, the contribution of water molecules is large and negative (*cf.* with ref. 66) and increases with the number of deprotonated (anionic) fatty acids in the system, see Fig. S3 (ESI†). The only exception is the neutral SC bilayer with fully protonated FAs: the water contribution for this system is small and positive, and the corresponding profile develops a peak aimed to compensate the partial charges of ceramide molecules, see Fig. S3 (ESI†).

These observations can be complemented by analyzing the deuterium order parameter as presented in Fig. S4 (ESI†) for the fatty acid chain (F24) of ceramides and for the fatty acid chains of LAs and LAPs. The immediate observation is that the order parameter for the Cer F24 chain is practically independent of FA protonation. It is characterized by small values for carbon atoms close to the lipid/water interface, by the plateau and by a sharp drop within the tail end in line with ref. 32. As for the chains of free fatty acids LAs and LAPs, LAs are somewhat more disordered in the vicinity of the lipid/water interface.

However, starting from carbon C8, the LA chains are systematically more ordered compared to their protonated counterparts (LAPs), see Fig. S4 (ESI<sup>†</sup>). This is most likely due to more elongated conformations of LAs, which decrease the interdigitation of LA chains close to the middle of the SC bilayer. It has to be emphasized that the observed deprotonation-dependent ordering of fatty acid chains is in a good qualitative agreement with the results of previous computational and experimental studies.<sup>32,67</sup>

### 3.2 Energetics of cellulose–stratum corneum binding

We first focus on characterizing the cellulose–SC bilayer interactions by using umbrella sampling and compute the free energy of binding between the SC bilayer and the crystalline cellulose surface for all salt-free systems with different content of protonated FAs, see Fig. 3(a). The distance along the z-axis (the bilayer normal) between the COMs of the crystal and the bilayer was used as the reaction coordinate.

Fig. 3(a) shows a striking difference in the free energy profiles for the CEL–SC–100–PMF system and the rest of the systems which have a non-zero content of deprotonated fatty acids LAs: deprotonation promotes repulsion between the cellulose crystal and the SC, starting already at  $z = 6$  nm. The origin of this behavior

is most likely the anionic surface charge due to deprotonation. This is supported by the fact that the above mentioned increase in free energy is not observed for the CEL–SC–100–PMF system, the only system with uncharged SC bilayer.

Importantly, the free energy profiles for the CEL–SC systems with anionic SC bilayers depend strongly on the amount of deprotonated LAs. At high LA content (CEL–SC–P0–PMF and CEL–SC–P25–PMF), the electrostatic repulsion is strong and the free energy gradually increases upon approaching the cellulose surface and there is no binding. At smaller LA contents (CEL–SC–P50–PMF and CEL–SC–P75–PMF), the free energy profile develops a well in the vicinity of the cellulose surface, implying cellulose–stratum corneum attraction, Fig. 3(a). The microscopic origin of this behavior is hydrogen bonding as will be shown in detail in the next section.

Overall, the free energy profiles clearly show that the cellulose–stratum corneum interactions are controlled by two major factors: (i) electrostatic repulsion between the cellulose surface and the SC bilayer due to deprotonation of free fatty acids and (ii) cellulose–SC binding due to hydrogen bonding. Interplay of these two factors controls the precise nature of the interactions. When most fatty acids are deprotonated (LA content of 75% and higher), the cellulose-based biomaterial does not bind to the skin. In contrast, increase in FA protonation promotes the cellulose–SC binding, so that the strongest interactions are observed for a system with fully protonated FAs (the CEL–SC–P100–PMF system). The depths of the free energy minima were found to be  $-16$ ,  $-47$ , and  $-127$  kJ mol<sup>-1</sup> for the CEL–SC–P50–PMF, CEL–SC–P75–PMF, and CEL–SC–P100–PMF systems, respectively, see Fig. 3(a). When normalized by the number of cellulose dimers (72) on the surface of the crystal, these yield correspondingly  $-0.22$ ,  $-0.65$ , and  $-1.76$  kJ mol<sup>-1</sup>. Interestingly, the free energy of binding of cellulose and a SC bilayer with fully protonated FAs turned out to be rather close to the results found for phosphatidylcholine ( $-1.89$  kJ mol<sup>-1</sup>) and phosphatidylethanolamine ( $-1.96$  kJ mol<sup>-1</sup>) lipid bilayers.<sup>16,17</sup> The free energy minima are located at 4 nm (the CEL–SC–P50–PMF system) and 3.8 nm (the CEL–SC–P75–PMF and CEL–SC–P100–PMF systems), showing that the closer the distance the stronger the binding.

Since the CEL–SC systems contain charged species (deprotonated FAs), it is important to evaluate the possible effects of salt ions on the free energy of binding. We chose two CEL–SC systems with different binding behavior and added KCl salt of physiological concentration (150 mM), see the CEL–SC–P25–KCl–PMF and CEL–SC–P50–KCl–PMF systems in Table 1. The results are shown in Fig. 3(b) and they demonstrate that the presence of salt leads to screening of the SC bilayer charge at longer distances. At small distances the behaviors of salt-free and saline systems are surprisingly similar. A reason for that is fairly straightforward: when a SC bilayer approaches the cellulose surface, salt ions tend to leave the contact area due to entropy gain. The only exception are the K<sup>+</sup> counterions that are bound tightly to the lipid/water interface. Since the amount bound ions is dictated by the overall surface charge of the SC bilayer, it is more or less the same for salt-free and saline systems.

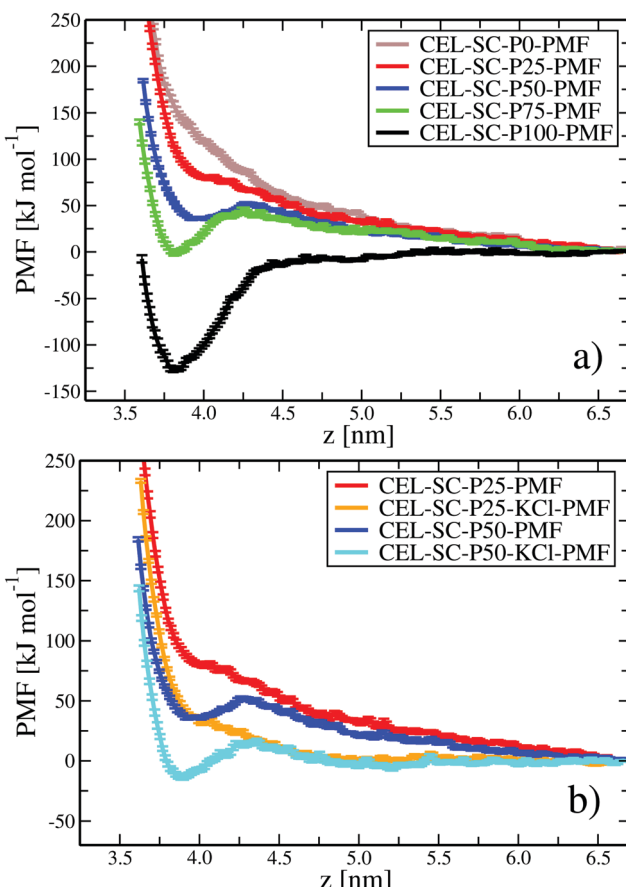


**Fig. 3** (a) Free-energy profiles for the binding of SC lipid bilayers to the surface of a cellulose crystal. The reaction coordinate was chosen to be the distance along the z-axis (the bilayer normal) between the centers of mass of the SC bilayer and the cellulose crystal. (b) Free-energy profiles for the systems with KCl salt and their salt-free counterparts.

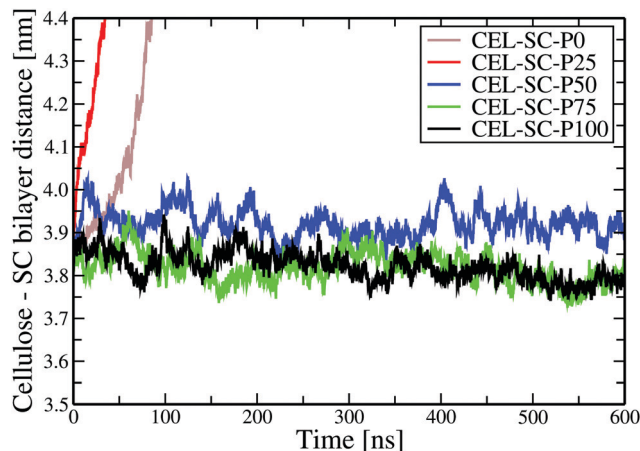


Fig. 4 Distance between the centers of mass of SC lipid bilayers and a cellulose crystal along the  $z$ -axis (the bilayer normal) as a function of time.

In addition to the umbrella sampling calculations, we performed unbiased MD simulations of five salt-free CEL-SC systems, Table 1. The starting configurations for the unbiased simulations corresponded to the crystal–bilayer distance of 3.8 nm, when the bilayer and the crystal have established a contact. This initial cellulose–SC distances approximately coincide with the locations of the free energy minima observed for the CEL-SC-P50–PMF, CEL-SC-P75–PMF, CEL-SC-P100–PMF systems, see Fig. 3.

Fig. 4 shows the time evolution of the distance between the COMs of the lipid bilayers and the cellulose crystals along the bilayer normal. The results are fully consistent with the biased simulations: the cellulose surface and the SC bilayers with high (75 and 100%) content of deprotonated FAs demonstrate the overall electrostatic repulsion in line with the free energy profiles, see Fig. 3(a) and 4. In great contrast, the systems in which the free energy well is present in the vicinity of the cellulose surface indeed show cellulose–SC attraction: the bilayer and the crystal stay in contact during the simulation course, see Fig. 4. Importantly, the average cellulose–SC distance amounts to  $3.92 \pm 0.01$ ,  $3.81 \pm 0.01$ , and  $3.80 \pm 0.01$  nm for the systems with 50, 75, and 100% of protonated FAs, which correlates perfectly with the corresponding positions of the free energy minima in Fig. 3(a).

Since the cellulose–SC bilayer binding does not require any biasing potential when the FA protonation is high, the unbiased simulations of the CEL-SC-P50, CEL-SC-P75, CEL-SC-P100 systems will be used in next section to analyze the structure of the cellulose–*stratum corneum* interfacial region and to identify the chemical groups of cellulose and components of the SC bilayer, which are responsible for this tight binding. The last 300 ns of 600 ns MD trajectories will be used for the analysis.

### 3.3 Cellulose–*stratum corneum* interactions upon binding

Fig. 5 shows the mass density profiles for three cellulose–SC bilayer systems (CEL-SC-P50, CEL-SC-P75, and CEL-SC-P100), for which the strong attractive interactions are observed. First off, one can notice a slight disturbance in the mass density profile of the SC bilayer, which makes the profile non-symmetric, especially for the CEL-SC-P75 and CEL-SC-P100 systems (*cf.* with Fig. S1, ESI<sup>†</sup>).

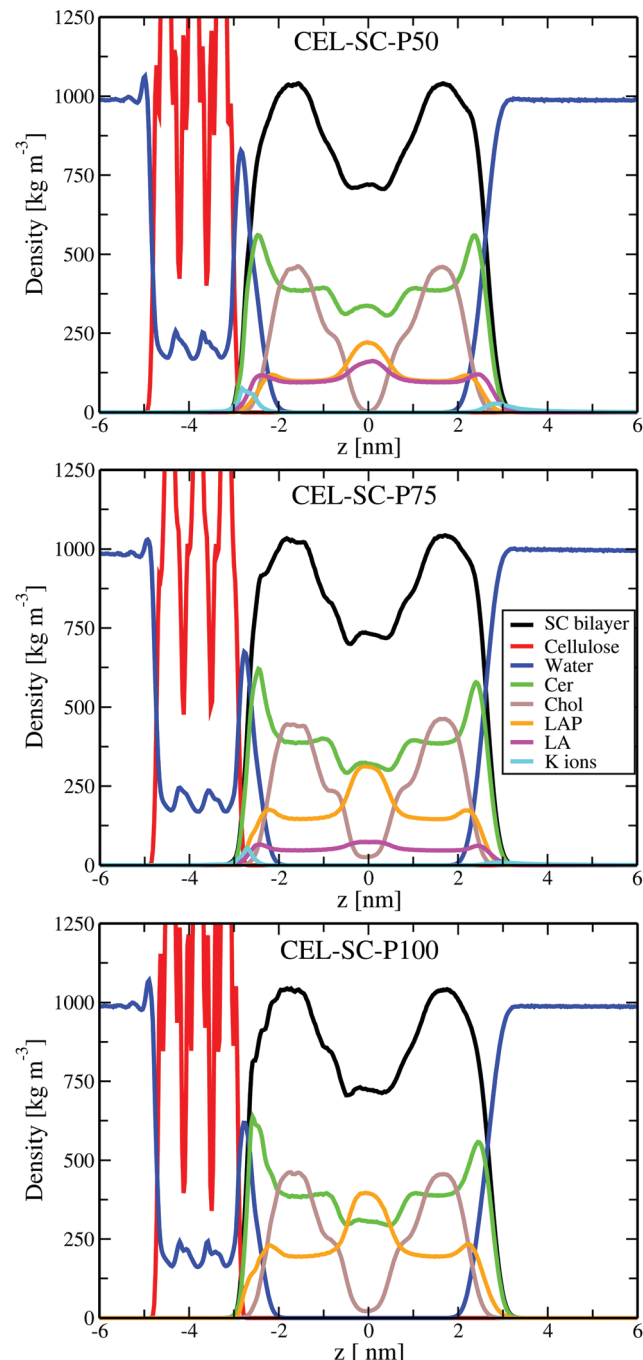
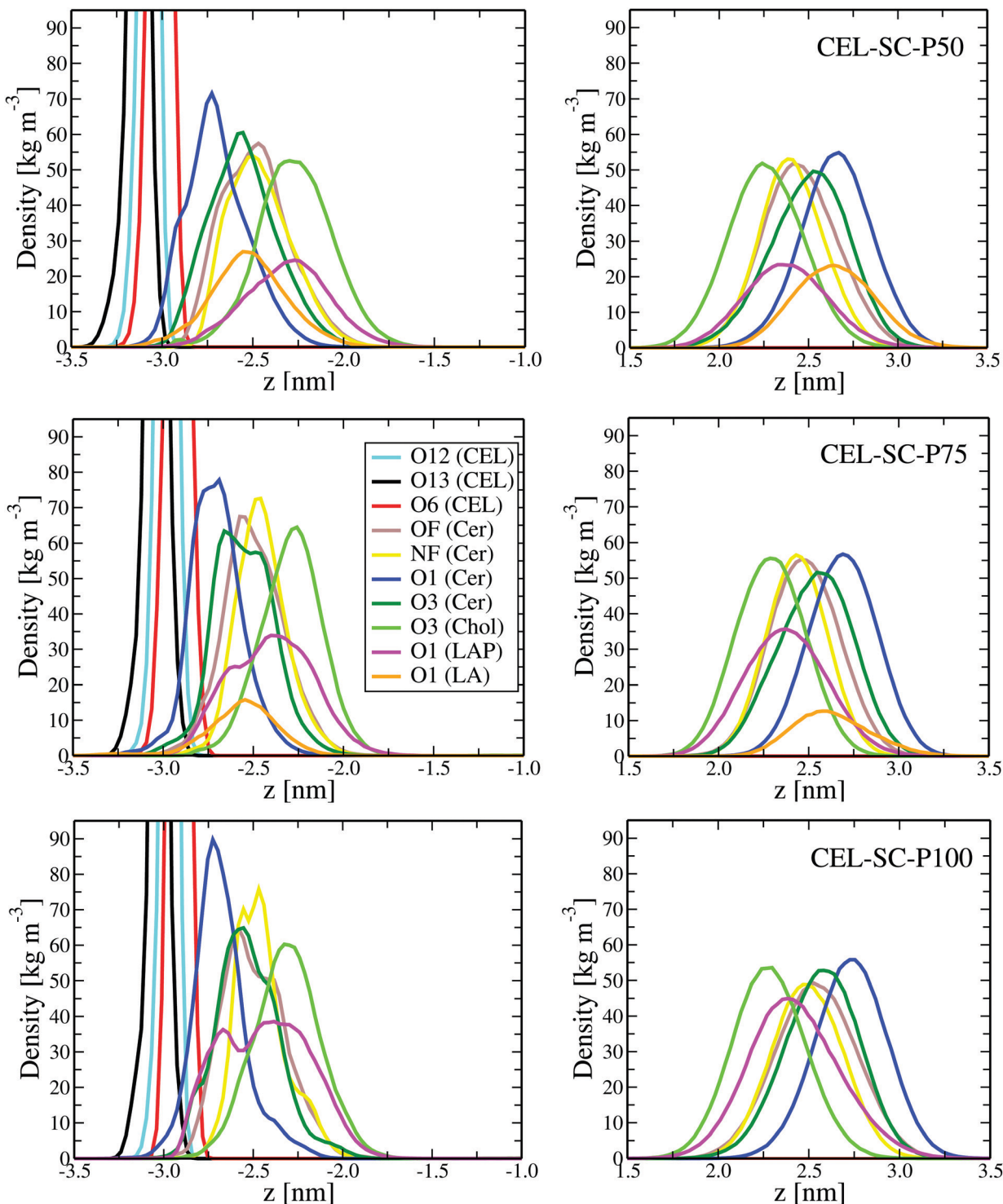


Fig. 5 Mass density profiles for cellulose crystals, SC lipid bilayers, water, and  $\text{K}^+$  counterions as a function of distance from the SC bilayer center ( $z = 0$ ).

This asymmetry is most pronounced for ceramides, because the mass density profiles of the whole SC bilayer and of the Cer molecules in the bilayer/water interface practically coincide, see Fig. 5 and Fig. S1 (ESI<sup>†</sup>). Indeed, for the CEL-SC-P75 and CEL-SC-P100 systems the peaks of mass density distributions of Cer are somewhat higher in the leaflet proximal to the cellulose crystal. In addition, there is a noticeable dehydration of the cellulose–*stratum corneum* interfacial region, when FA protonation content increases from 50 to 75%, see Fig. 5. It is also noteworthy that for

in the CEL-SC-P50 system the protonated FAs do not interact with cellulose in contrast to their deprotonated counterparts; LAs are kept in the lipid–water interface by electrostatic interactions with  $K^+$  counter-ions bound to the SC bilayer surface. Further increase in the content of protonated FAs enhances the role of LAPs in the cellulose–SC interactions.

To gain a more detailed insight into the cellulose–SC bilayer interactions, Fig. 6 shows the component-wise mass density profiles for the key atoms of cellulose, ceramides, fatty acids, and cholesterol. To aid comparison, the SC bilayer leaflets that are proximal and distal to the cellulose surface are shown separately. The figure shows that the mass density profiles of



**Fig. 6** Component-wise mass density profiles for key atoms of cellulose, ceramides, fatty acids, and cholesterol as a function of the distance from the SC bilayer center for the CEL-SC-P50, CEL-SC-P75, and CEL-SC-P100 systems. Left: Proximal leaflets. Right: Distal leaflets.

all key atomic groups are influenced. Even cholesterol molecules, being the most buried into the bilayer and therefore the least involved species in cellulose–SC interactions, are affected: the peaks of the mass density profiles of cholesterol's hydroxyl oxygens groups (O3) are somewhat higher in the proximal leaflet, Fig. 6.

As can already be expected from Fig. 5, the mass distributions of ceramides are strongly influenced by the cellulose surface. The mass density profiles of ceramide hydroxyl groups (O1) have the largest overlap (the strongest interactions) with the cellulose atoms (labeled CEL), see Fig. 6. In turn, the ceramide nitrogen atoms (NF) do not participate in cellulose–SC interactions.

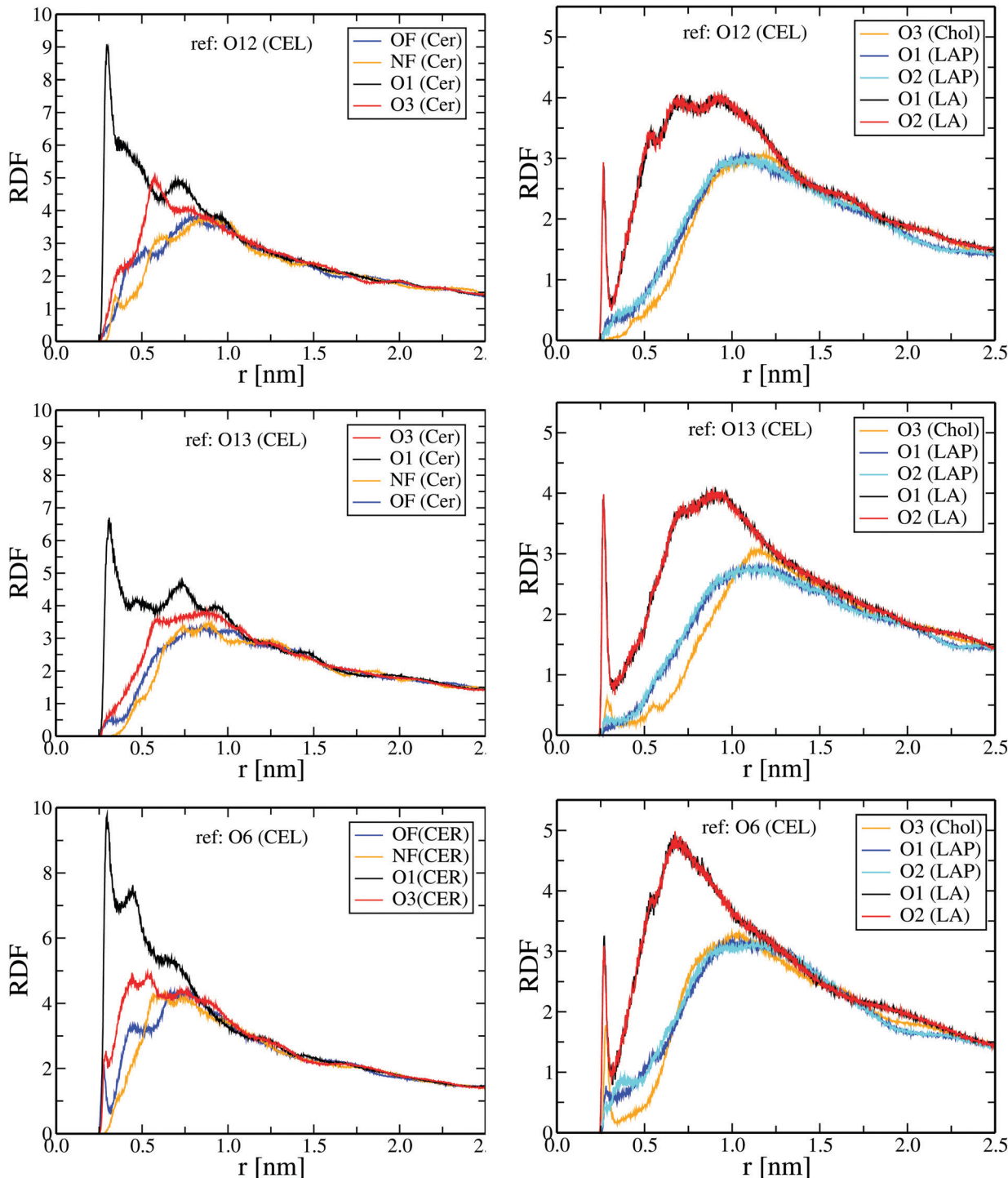


**Fig. 7** Radial distribution functions (RDFs) of cellulose's oxygen atoms (O12, O13, and O6) and principal atoms of ceramides (left) and of fatty acids and cholesterol (right). Shown are results for the CEL–SC–P50 system. RDFs for the CEL–SC–P75 and CEL–SC–P100 systems are presented in Fig. S5 and S6 (ESI†).

The hydroxyl groups (O3) and the oxygen atoms (OF) demonstrate an intermediate behavior: O3 is located somewhat closer to the bilayer surface than OF although their density profiles coincide for the system with fully protonated FAs. As for the FA densities, the profiles for deprotonated LAs stays almost the same for both proximal and distal leaflets. In contrast, the density distribution of protonated LAPs develops a second peak upon increasing FA protonation, indicating strong cellulose–FA interactions of some of the LAPs in the CEL–SC-P100 system, see Fig. 6.

Another way to characterize the cellulose–SC interactions and the structure of the interfacial region is to compute radial distribution functions (RDFs) for the key atoms of the systems at hand. In Fig. 7 and Fig. S5, S6 (ESI<sup>†</sup>) we show RDFs of cellulose's hydroxyl (hydroxymethyl) groups O12, O13, and O6 with principal atoms of SC bilayer components for the CEL–SC-P50, CEL–SC-P75, and CEL–SC-P100 systems, respectively (see Fig. 2 for atom numbering).

As can be expected from the density profiles (Fig. 6), the highest RDF peaks for ceramide atoms (the strongest interactions with cellulose atoms) are observed for the ceramide's hydroxyl groups O1. Furthermore, noticeable RDF peaks also develop for ceramide oxygen atoms O3 and OF, when all FAs are protonated, see Fig. S6 (ESI<sup>†</sup>). In turn, cholesterol's hydroxyl group O3, being located deep in the SC bilayer leaflets, does not show any RDF peaks with key cellulose atoms. As for the free fatty acids, oxygen atoms O1 and O2 of deprotonated LAs dominate in the interactions with cellulose, see Fig. 7 and Fig. S5 (ESI<sup>†</sup>). The RDFs of oxygen atoms of protonated LAPs also develop peaks when the LAP content amounts to 75%, especially for the cellulose's hydroxymethyl groups O6, see Fig. S5 (ESI<sup>†</sup>). Furthermore, one can witness strong LAP–cellulose interactions, when all free fatty acids are protonated (Fig. S6, ESI<sup>†</sup>).

To further characterize the cellulose–stratum corneum interactions, we analyzed hydrogen bonding between the cellulose and the SC lipid bilayer. This type of interactions can play a crucial role, because the cellulose surface and most components of SC bilayers (Cer, Chol, and LAP) have hydroxyl groups which can be both donors and acceptors of hydrogen bonds. To analyze the cellulose–SC bilayer hydrogen bonding we used the following definition: the donor–acceptor distance was smaller than 0.35 nm and the hydrogen donor–acceptor angle did not exceed 30°. Table 2 summarizes the average numbers of hydrogen bonds (the results are normalized by the number of cellulose dimers on the crystal surface (72 dimers)).

The data in Table 2 shows that cellulose–stratum corneum hydrogen bonding is indeed very strong: it increases with FA protonation and reaches the maximal value of 0.64 hydrogen bonds/cellulose dimer, when all fatty acids in the SC bilayer are

**Table 2** Number of hydrogen bonds between cellulose and SC bilayers, and between cellulose and SC bilayers' components (per cellulose dimer)

	CEL–SC-P50	CEL–SC-P75	CEL–SC-P100
CEL–SC bilayer	0.274 ± 0.006	0.58 ± 0.02	0.64 ± 0.01
CEL–Cer	0.212 ± 0.006	0.44 ± 0.01	0.417 ± 0.006
CEL–LAP	0.005 ± 0.001	0.069 ± 0.004	0.213 ± 0.007
CEL–LA	0.046 ± 0.003	0.065 ± 0.004	—
CEL–Chol	0.011 ± 0.003	0.009 ± 0.002	0.010 ± 0.001

protonated. Remarkably, the major contribution in the cellulose–SC hydrogen bonding comes from ceramide molecules, although protonated LAPs also contribute substantially in the CEL–SC-P100 system. The contribution of cholesterol molecules is negligible since they are buried in the SC bilayer.

Interestingly, the relative contribution of protonated and deprotonated fatty acids to hydrogen bonding depend on the relative content of LAs and LAPs. For the system with an equimolar mixture of LAs and LAPs, most cellulose–FA hydrogen bonds are due to deprotonated fatty acids: anionic LAs are more elongated toward the water phase, where they interact with adsorbed K<sup>+</sup> counterions. Furthermore, the CEL–SC-P50 system is characterized by the largest average cellulose–SC bilayer distance among the three systems (see Fig. 4), preventing thereby hydrogen bonding between LAPs and cellulose. When the LAP content amounts to 75%, the cellulose and the bilayer establish a closer contact and the contributions of LAs and LAPs become comparable (note however that the number of protonated FAs is three times larger than that of their deprotonated counterparts for the CEL–SC-P75 system). For the system with fully protonated FAs, one third of all cellulose–stratum corneum hydrogen bonds are formed by LAPs, see Table 2.

A more detailed insight into the cellulose–SC bilayer hydrogen bonding is presented in Table 3. In line with the results for RDFs,

**Table 3** Number of hydrogen bonds between principal groups of cellulose and SC bilayer's components (per cellulose dimer)

	O12 (CEL)	O13 (CEL)	O6 (CEL)
OF (Cer)–cellulose			
CEL–SC-P50	0.0014 ± 0.0002	0.0016 ± 0.0003	0.010 ± 0.001
CEL–SC-P75	0.020 ± 0.002	0.011 ± 0.001	0.026 ± 0.002
CEL–SC-P100	0.0059 ± 0.0009	0.016 ± 0.002	0.035 ± 0.002
NF (Cer)–cellulose			
CEL–SC-P50	0.0002 ± 0.0001	0	0.0003 ± 0.0001
CEL–SC-P75	0.0002 ± 0.0001	0.0001 ± 0.0001	0.0016 ± 0.0004
CEL–SC-P100	0.0001 ± 0.0001	0	0.0039 ± 0.0006
O1 (Cer)–cellulose			
CEL–SC-P50	0.060 ± 0.005	0.0313 ± 0.0009	0.064 ± 0.002
CEL–SC-P75	0.130 ± 0.004	0.051 ± 0.003	0.113 ± 0.002
CEL–SC-P100	0.120 ± 0.003	0.046 ± 0.001	0.090 ± 0.002
O3 (Cer)–cellulose			
CEL–SC-P50	0.0039 ± 0.0004	0.0023 ± 0.0005	0.013 ± 0.002
CEL–SC-P75	0.013 ± 0.001	0.0079 ± 0.0008	0.025 ± 0.002
CEL–SC-P100	0.044 ± 0.001	0.0060 ± 0.0007	0.015 ± 0.001
O1 (LAP)–cellulose			
CEL–SC-P50	0.0008 ± 0.0001	0.0003 ± 0.0001	0.0017 ± 0.0002
CEL–SC-P75	0.0116 ± 0.0009	0.007 ± 0.001	0.025 ± 0.001
CEL–SC-P100	0.030 ± 0.001	0.038 ± 0.002	0.063 ± 0.003
O2 (LAP)–cellulose			
CEL–SC-P50	0.0003 ± 0.0001	0.0007 ± 0.0001	0.0010 ± 0.0002
CEL–SC-P75	0.009 ± 0.001	0.0043 ± 0.0004	0.0112 ± 0.0007
CEL–SC-P100	0.040 ± 0.002	0.018 ± 0.001	0.023 ± 0.001
O1 (LA)–cellulose			
CEL–SC-P50	0.0058 ± 0.0007	0.0086 ± 0.0007	0.0073 ± 0.0009
CEL–SC-P75	0.0098 ± 0.0007	0.012 ± 0.001	0.0064 ± 0.0006
CEL–SC-P100	—	—	—
O2 (LA)–cellulose			
CEL–SC-P50	0.0056 ± 0.0006	0.0083 ± 0.0007	0.0069 ± 0.0008
CEL–SC-P75	0.0107 ± 0.0008	0.012 ± 0.001	0.0065 ± 0.0008
CEL–SC-P100	—	—	—
O3 (Chol)–cellulose			
CEL–SC-P50	0	0.0028 ± 0.0007	0.008 ± 0.002
CEL–SC-P75	0.003 ± 0.001	0.0015 ± 0.0004	0.004 ± 0.001
CEL–SC-P100	0.0027 ± 0.0006	0.0023 ± 0.0003	0.005 ± 0.001

the hydroxyl group O1 of ceramides dominates in the ceramide–cellulose hydrogen bonding; the strongest bonding is observed for O12 and O6 hydroxyl groups of cellulose. The contributions of ceramide's oxygen atoms OF and O3 are considerably smaller, while nitrogen atoms NF do not participate in the hydrogen bonding. The contribution of cholesterol molecules is also negligible. It is noteworthy that contributions of LAP's oxygen atoms O1 and O2 are not equivalent, as far as the hydrogen bonding is concerned. The oxygen atom O1 of a protonated fatty acid belongs to hydroxyl group, which can be both donors and acceptors of hydrogen bonds. Therefore, the number of hydrogen bonds associated with atoms O1 of LAPs is systematically larger than that for LAP's atoms O2, see Table 3. In turn, both oxygen atoms O1 and O2 of deprotonated fatty acids LAs can serve only as acceptors of hydrogen bonds, so that their contributions to the hydrogen bonding are very similar (Table 3). Overall, the hydrogen bonding plays a crucial role the cellulose–skin binding, provided that at least half of free fatty acids in the SC bilayer are protonated.

## 4 Conclusions

Cellulose–skin interactions are a central issue in many biomedical applications of cellulose-based materials, which often involve a direct contact between a biomaterial and a living tissue, and skin in particular. Thus, being able to tune and control biomaterial–skin/tissue interactions, molecular-level insight into the detailed physical mechanisms is critical yet currently lacking.

In this work, we employed both biased and unbiased atomic-scale molecular dynamics simulations to study a cellulose crystal interacting with a model *stratum corneum* bilayer that mimics the extracellular lipid matrix of the outermost layer of the skin. The SC bilayer comprised an equimolar mixture of ceramides, cholesterol and free fatty acids. We focused on the role of acidity in the cellulose–SC bilayer contact area. As the acidity is directly linked to protonation of fatty acids, we varied systematically the content of protonated FAs in the bilayer and considered SC lipid bilayers with 0, 25, 50, 75, and 100% of protonated fatty acids. This allowed us to explore, for the first time, the impact of fatty acid protonation on cellulose–skin interactions.

Our results show that acidity, *via* protonation, in the contact area directly controls binding between the cellulose-based material and the *stratum corneum* bilayer: tight cellulose–skin binding was observed when at least half of fatty acids in the bilayer are protonated. Overall, we identified two major physical mechanisms in cellulose–skin interactions: (i) electrostatic repulsion between the cellulose crystal and the SC bilayer, whose surface is anionic due to the presence of deprotonated fatty acids and (ii) cellulose–*stratum corneum* hydrogen bonding. At small content of protonated fatty acids the first factor dominates, so that the cellulose biomaterial does not attach to the skin. In turn, an increase in FA protonation reduces the anionic charge of the SC bilayer and elevates the role of hydrogen bonding in cellulose–skin interactions. It is therefore not surprising that the strongest binding of a cellulose crystal to a SC lipid bilayer is observed for a system with fully protonated

fatty acids. The corresponding free energy of binding was found to be  $-1.76 \text{ kJ mol}^{-1}$  per cellulose dimer, which is rather close to the energies computed previously for model plasma membranes.<sup>16</sup> It is also noteworthy that not all components of the SC lipid bilayer participate equally in cellulose–*stratum corneum* hydrogen bonding. The major portion of the hydrogen bonds is due to ceramide molecules, while cholesterol, being buried in the interior of the bilayer leaflets, is not involved in hydrogen bonding. The role of protonated fatty acids increases with the protonation level, so that one third of all cellulose–SC hydrogen bonds are formed by protonated fatty acids in systems in which only protonated FAs are present.

To link our findings to real SC, we recall that there is a pH gradient in SC layers, from acidic pH (4.5–5.3) in the outer layer to almost neutral pH (6.8) in the inner layers.<sup>68</sup> In turn,  $pK_a$  of lignoceric acid is around 4.95 (*i.e.* close to pH in the outer layer), which implies that approximately half of LA molecules on the outer surface of the skin are protonated. Our computational findings indicate that at such FA protonation level one has adhesion between the cellulose-based material and the skin (the CEL–SC–P50–PMF system). To weaken this adhesion, one needs to increase pH in the contact area in order to make the SC bilayer anionic and thus promote repulsion between the biomaterial and the skin.

It is noteworthy that in our study we used the crystal structure of I $\beta$  cellulose. Crystalline native cellulose has also another form, I $\alpha$ . It is known that I $\beta$  cellulose has a monoclinic unit cell, while I $\alpha$  cellulose has a triclinic one.<sup>69</sup> This difference mainly concerns the inner organization of the cellulose crystals. However, when it comes to the density of hydroxyl groups on the surface of a cellulose crystal (and, correspondingly, to the ability of the crystal surface to form hydrogen bonds), the difference between I $\alpha$  and I $\beta$  cellulose is negligible, so that our findings also hold for I $\alpha$  cellulose. Furthermore, here, we have used a simple model SC. Real SC is, however, complex, see *e.g.* the discussions in ref. 38 and 70. It would be very interesting to extend the current study to more complex models that include variations in SC that depend on anatomical site in the body as discussed by Mohammed *et al.*<sup>70</sup> The main characteristics of such variations could potentially be included in a large-scale computational model to study, for example, drug permeability.

In summary, our study highlights the critical role of acidity in the interactions of the outer layers of skin with cellulose (and possibly with any other biomaterials whose surface is capable of hydrogen bonding). In particular, our computational findings can be used for optimizing surface properties of cellulose-based materials aimed at the use in wound dressings.

## Author contributions

Andrey A. Gurtovenko: conceptualization, methodology, investigation, validation, formal analysis, writing – original draft, project administration, visualization. Mikko Karttunen: conceptualization, investigation, validation, formal analysis, writing – review and editing, funding acquisition.

## Conflicts of interest

There are no conflicts to declare.

## Acknowledgements

This work was supported by the Russian Ministry of Education and Science within state contract 14.W03.31.0014 (MegaGrant). The authors acknowledge the use of the SHARCNET/Compute Canada computing facilities (Canada) and the computer cluster at the Institute of Macromolecular Compounds RAS (Russia).

## Notes and references

- 1 A. Dufresne, *Mater. Today*, 2013, **16**, 220–227.
- 2 M. Gunnoo, P.-A. Cazade, A. Galera-Prat, M. A. Nash, M. Czjzek, M. Cieplak, B. Alvarez, M. Aguilar, A. Karpol, H. Gaub, M. Carrión-Vázquez, E. A. Bayer and D. Thompson, *Adv. Mater.*, 2016, **28**, 5619–5647.
- 3 J. Majoinen, J. Hassinen, J. S. Haataja, H. T. Rekola, E. Kontturi, M. A. Kostiainen, R. H. A. Ras, P. Törmä and O. Ikkala, *Adv. Mater.*, 2016, **28**, 5262–5267.
- 4 A. P. C. Almeida, J. P. Canejo, S. N. Fernandes, C. Echeverria, P. L. Almeida and M. H. Godinho, *Adv. Mater.*, 2018, **30**, 1703655.
- 5 J. S. Yang and J. F. Li, *Carbohydr. Polym.*, 2018, **181**, 264–274.
- 6 R. J. Hickey and A. E. Pelling, *Front. Bioeng. Biotechnol.*, 2019, **7**, 45.
- 7 B. L. Peng, N. Dhar, H. L. Liu and K. C. Tam, *Can. J. Chem. Eng.*, 2011, **89**, 1191–1206.
- 8 X. G. Lv, J. X. Yang, C. Feng, Z. Li, S. Y. Chen, M. K. Xie, J. W. Huang, H. B. Li, H. P. Wang and Y. M. Xu, *ACS Biomater. Sci. Eng.*, 2016, **2**, 19–29.
- 9 N. O'Donnell, I. A. Okkelman, P. Timashev, T. I. Gromovych, D. B. Papkovsky and R. I. Dmitriev, *Acta Biomater.*, 2018, **80**, 85–96.
- 10 D. A. Osorio, B. E. J. Lee, J. M. Kwiecien, X. Wang, I. Shahid, A. L. Hurley, E. D. Cranston and K. Grandfield, *Acta Biomater.*, 2019, **87**, 152–165.
- 11 K. Kokubo, Y. Kurihara, K. Kobayashi, H. Tsukao and H. Kobayashi, *Blood Purif.*, 2015, **40**, 293–297.
- 12 C. Ronco and W. R. Clark, *Nat. Rev. Nephrol.*, 2018, **14**, 394–410.
- 13 J. S. Boateng, K. H. Matthews, H. N. E. Stevens and G. M. Eccleston, *J. Pharm. Sci.*, 2008, **97**, 2892–2923.
- 14 M. R. Prausnitz, S. Mitragotri and R. Langer, *Nat. Rev. Drug Discovery*, 2004, **3**, 115–124.
- 15 A. Y. Kostritskii, D. A. Tolmachev, N. V. Lukasheva and A. A. Gurtovenko, *Langmuir*, 2017, **33**, 12793–12803.
- 16 A. A. Gurtovenko, E. I. Mukhamadiarov, A. Y. Kostritskii and M. Karttunen, *J. Phys. Chem. B*, 2018, **122**, 9973–9981.
- 17 A. A. Gurtovenko and M. Karttunen, *Langmuir*, 2019, **35**, 13753–13760.
- 18 M. L. Williams and P. M. Elias, *Crit. Rev. Ther. Drug Carrier Syst.*, 1987, **3**, 95–122.
- 19 P. W. Wertz and D. T. Downing, *Adv. Drug Delivery Rev.*, 1996, **18**, 283–294.
- 20 L. Norlen, I. Nicander, B. L. Rozell, S. Ollmar and B. Forslind, *J. Invest. Dermatol.*, 1999, **112**, 72–77.
- 21 A. Weerheim and M. Ponec, *Arch. Dermatol. Res.*, 2001, **293**, 191–199.
- 22 K. C. Madison, *J. Invest. Dermatol.*, 2003, **121**, 231–241.
- 23 T. Engelbrecht, A. Schroeter, T. Hauss, B. Deme, H. Scheidt, D. Huster and R. Neubert, *Soft Matter*, 2012, **8**, 6599–6607.
- 24 M. Rabionet, K. Gorgas and R. Sandhoff, *Biochim. Biophys. Acta*, 2014, **1841**, 422–434.
- 25 E. Wang and J. B. Klauda, *J. Am. Chem. Soc.*, 2019, **141**, 16930–16943.
- 26 S. A. Pandit and H. L. Scott, *J. Chem. Phys.*, 2006, **124**, 14708.
- 27 R. Notman, J. Anwar, W. J. Briels, M. G. Noro and W. K. den Otter, *Biophys. J.*, 2008, **95**, 4763–4771.
- 28 S. Guo, T. C. Moore, C. R. Iacobella, L. A. Strickland and C. McCabe, *J. Chem. Theory Comput.*, 2013, **9**, 5116–5126.
- 29 R. Gupta and B. Rai, *J. Phys. Chem. B*, 2015, **119**, 11643–11655.
- 30 R. Gupta, D. B. Sridhar and B. Rai, *J. Phys. Chem. B*, 2016, **120**, 8987–8996.
- 31 E. Wang and J. B. Klauda, *J. Phys. Chem. B*, 2018, **122**, 2757–2768.
- 32 E. Wang and J. B. Klauda, *J. Phys. Chem. B*, 2018, **122**, 11996–12008.
- 33 T. C. Moore, R. Hartkamp, C. R. Iacobella, A. L. Bunge and C. McCabe, *Biophys. J.*, 2018, **114**, 113–125.
- 34 P. M. Elias, *Exp. Dermatol.*, 2015, **24**, 179–180.
- 35 Y. Nishiyama, P. Langan and H. Chanzy, *J. Am. Chem. Soc.*, 2002, **124**, 9074–9082.
- 36 R. R. Warner, M. C. Myers and D. A. Taylor, *J. Investig. Dermatol.*, 1988, **90**, 218–224.
- 37 C. Silva, D. Topgaard, V. Kocherbitov, J. Sousa, A. Pais and E. Sparr, *Biochim. Biophys. Acta, Biomembr.*, 2007, **1768**, 2647–2659.
- 38 E. H. Mojumdar, Q. D. Pham, D. Topgaard and E. Sparr, *Sci. Rep.*, 2017, **7**, 15712.
- 39 M. Höltje, T. Förster, B. Brandt, T. Engels, W. von Rybinski and H.-D. Höltje, *Biochim. Biophys. Acta, Biomembr.*, 2001, **1511**, 156–167.
- 40 M. Roark and S. E. Feller, *Langmuir*, 2008, **24**, 12469–12473.
- 41 C. Y. Xing and R. Faller, *J. Phys. Chem. B*, 2008, **112**, 7086–7094.
- 42 C. M. Hartshorn, C. M. Jewett and J. A. Brozik, *Langmuir*, 2010, **26**, 2609–2617.
- 43 O. Guvench, S. N. Greene, G. Kamath, J. W. Brady, R. M. Venable, R. W. Pastor and A. D. MacKerell, *J. Comput. Chem.*, 2008, **29**, 2543–2564.
- 44 O. Guvench, E. Hatcher, R. M. Venable, R. W. Pastor and A. D. MacKerell, *J. Chem. Theory Comput.*, 2009, **5**, 2353–2370.
- 45 J. B. Klauda, R. M. Venable, J. A. Freites, J. W. O'Connor, D. J. Tobias, C. Mondragon-Ramirez, I. Vorobyov, A. D. MacKerell and R. W. Pastor, *J. Phys. Chem. B*, 2010, **114**, 7830–7843.
- 46 R. M. Venable, A. J. Sodt, B. Rogaski, H. Rui, E. Hatcher, A. D. MacKerell, R. W. Pastor and J. B. Klauda, *Biophys. J.*, 2014, **107**, 134–145.

- 47 A. D. MacKerell, D. Bashford, M. Bellott, R. L. Dunbrack, J. D. Evanseck, M. J. Field, S. Fischer, J. Gao, H. Guo, S. Ha, D. Joseph-McCarthy, L. Kuchnir, K. Kuczera, F. T. K. Lau, C. Mattos, S. Michnick, T. Ngo, D. T. Nguyen, B. Prodhom, W. E. Reiher, B. Roux, M. Schlenkrich, J. C. Smith, R. Stote, J. Straub, M. Watanabe, J. Wiorkiewicz-Kuczera, D. Yin and M. Karplus, *J. Phys. Chem. B*, 1998, **102**, 3586–3616.
- 48 M. J. Abraham, T. Murtola, R. Schulz, S. Pall, J. Smith, B. Hess and E. Lindahl, *SoftwareX*, 2015, **1–2**, 19–25.
- 49 G. Bussi, D. Donadio and M. Parrinello, *J. Chem. Phys.*, 2007, **126**, 014101.
- 50 H. J. C. Berendsen, J. P. M. Postma, A. DiNola and J. R. Haak, *J. Chem. Phys.*, 1984, **81**, 3684–3690.
- 51 S. Nosé, *Mol. Phys.*, 1984, **52**, 255–268.
- 52 W. G. Hoover, *Phys. Rev. A: At., Mol., Opt. Phys.*, 1985, **31**, 1695–1697.
- 53 M. Parrinello and A. Rahman, *J. Appl. Phys.*, 1981, **52**, 7182–7190.
- 54 M. R. Shirts, *J. Chem. Theory Comput.*, 2013, **9**, 909–926.
- 55 J. Wong-ekkabut and M. Karttunen, *Biochim. Biophys. Acta Biomembr.*, 2016, **1858**, 2529–2538.
- 56 B. Hess, *J. Chem. Theory Comput.*, 2008, **4**, 116–122.
- 57 U. Essman, L. Perera, M. L. Berkowitz, T. Darden, H. Lee and L. G. Pedersen, *J. Chem. Phys.*, 1995, **103**, 8577–8592.
- 58 S. Jo, T. Kim, V. G. Iyer and W. Im, *J. Comput. Chem.*, 2008, **29**, 1859–1865.
- 59 E. L. Wu, X. Cheng, S. Jo, H. Rui, K. C. Song, E. M. Davila-Contreras, Y. F. Qi, J. M. Lee, V. Monje-Galvan, R. M. Venable, J. B. Klauda and W. Im, *J. Comput. Chem.*, 2014, **35**, 1997–2004.
- 60 G. M. Torrie and J. P. Valleau, *J. Comput. Phys.*, 1977, **23**, 187–199.
- 61 J. S. Hub, B. L. de Groot and D. van der Spoel, *J. Chem. Theory Comput.*, 2010, **6**, 3713–3720.
- 62 S. Kumar, J. M. Rosenberg, D. Bouzida, R. H. Swendsen and P. A. Kollman, *J. Comput. Chem.*, 1992, **13**, 1011–1021.
- 63 L. R. Parisi, S. Sowlati-Hashjin, I. A. Berhane, S. L. Galster, K. A. Carter, J. F. Lovell, S. R. Chemler, M. Karttunen and G. E. Atilla-Gokcumen, *ACS Chem. Biol.*, 2019, **14**, 2286–2294.
- 64 A. A. Gurtovenko and I. Vattulainen, *J. Chem. Phys.*, 2009, **130**, 215107.
- 65 S. G. Falkovich, H. Martinez-Seara, A. M. Nesterenko, I. Vattulainen and A. A. Gurtovenko, *J. Phys. Chem. Lett.*, 2016, **7**, 4585–4590.
- 66 A. A. Gurtovenko and I. Vattulainen, *J. Phys. Chem. B*, 2009, **113**, 7194–7198.
- 67 A. P. Ramos, P. Lague, G. Lamoureux and M. Lafleur, *J. Phys. Chem. B*, 2016, **120**, 6951–6960.
- 68 J. W. Fluhr and P. M. Elias, *Exog. Dermatol.*, 2002, **1**, 163–175.
- 69 P. Zugenmaier, *Carbohydr. Polym.*, 2021, **254**, 117417.
- 70 D. Mohammed, P. J. Matts, J. Hadgraft and M. E. Lane, *AAPS J.*, 2012, **14**, 806–812.